

Self-Sacrificial Templatized Lithium Manganese Oxide as a Longevous Cathode: The Intermarriage of Oxygen Defects and Zeolitic Imidazolate Framework Glass

Jian-En Zhou, Yilin Li, Mingyan Zou, Xin Hu, Xinshuang Miao, Xinxian Xie, Xiaoming Lin,* Ji Qian, Chao Yang,* and Renjie Chen*

Spinel LiMn_2O_4 is a promising cathode material for lithium-ion batteries (LIBs) due to its nontoxicity, resource abundance, substantial operating voltage, and remarkable thermal stability. Nevertheless, LiMn_2O_4 is subjected to subpar electronic/ion conductivity and continuous capacity attenuation triggered by the Jahn-Teller distortion. In this regard, metal-organic frameworks (MOFs) are potential morphological controllers that impact particle size and crystal orientation and offer vacancy-accepting layers that facilitate oxygen defect formation, which boost electron/ion diffusion when utilized as self-sacrificial templates. The dissatisfying capacity retention caused by Mn^{2+} dissolution related to the Mn^{3+} disproportion is another tricky issue, which requires resolution through surface modification. To attain these goals, this work develops a strategy intermarrying the merits of oxygen defects and **Zn-based zeolitic imidazolate framework-62 (Zn-ZIF-62) glass shields**. Mn-MOFs with carboxyl-based ligands possessing various coordination numbers are adopted as precursors to optimize the morphological feature and modulate the oxygen vacancy level. Computational and experimental results examine the efficaciousness of oxygen defects in ameliorating the electrochemical activity and expediting electron/ion transportation. Synchronously, the ZIF-62 glass layer inhibits manganese loss and phase degradation toward prolonged cycling durability in LIB half/full cells. This study envisions a versatile methodology to modify spinel LiMn_2O_4 as a longevous cathode for next-generation LIBs.

1. Introduction

The development of advanced energy storage and conversion devices has become an utmost urgency since the depletion of fossil resources. To date, lithium-ion batteries (LIBs), as a landmark

technology, have dominated the energy market, whose key parameters including energy/power density, safety performance, and cyclability require more breakthroughs.^[1-3] To satisfy the growing demands for advanced LIBs, the exploitation of cathode materials is an ineluctable challenge since LIB cathodes are predominant for the overall battery performance.^[4,5] In this context, substantial endeavors have been dedicated to exploring and modifying cathode materials for next-generation LIBs.

Spinel LiMn_2O_4 , as a prevailing member of LIB cathodes, exhibits considerable reversible capacity (148 mAh g⁻¹), high operating voltage, excellent thermal stability, natural abundance, nontoxicity, and low manufacturing cost.^[6,7] These promising features render LiMn_2O_4 as a feasible alternative to LiCoO_2 , but LiMn_2O_4 encounters some drawbacks in its practice. Nevertheless, there remains sufficient room for improvement in the electronic/ion transmission kinetics of LiMn_2O_4 despite their impressive power density.^[8] Several strategies have been proposed for establishing successive conductive networks, such as carbon coating and conductive substrate support.^[9,10] Unfortunately, the adoption

of electrochemically inert conductive matrices severely tapers the energy density and is unfavorable for practical use. Other modification methods have also been developed to circumvent the fatal disadvantage of carbon-modified LiMn_2O_4 . For instance, the meticulous control of particle growth, morphological features,

J.-E. Zhou, Y. Li, M. Zou, X. Xie, X. Lin
 Guangzhou Key Laboratory of Materials for Energy Conversion and Storage
 Key Laboratory of Theoretical Chemistry of Environment
 Ministry of Education
 School of Chemistry
 South China Normal University
 Guangzhou 510006, P. R. China
 E-mail: linxm@scnu.edu.cn

X. Miao, C. Yang
 School of Environmental and Chemical Engineering
 Shanghai University
 Shanghai 200444, China
 E-mail: chaoyang@shu.edu.cn
 X. Hu, J. Qian, R. Chen
 Beijing Key Laboratory of Environmental Science and Engineering
 School of Material Science & Engineering
 Beijing Institute of Technology
 Beijing 100081, China
 E-mail: chenrj@bit.edu.cn

 The ORCID identification number(s) for the author(s) of this article can be found under <https://doi.org/10.1002/adfm.202501603>

DOI: 10.1002/adfm.202501603

and crystallinity is instrumental to the resulting electrochemical behaviors.^[7,11] The combinatorial adjustment of these parameters can enable the proper development and optimization of spinel materials. Aside from the macroscopical design, atomic-level modulation approaches such as cation substitution^[12,13] and oxygen vacancy engineering^[14–16] have been proposed to pursue the balanced merits of excellent lithium storage performance and satisfying energy/power density. Among them, oxygen vacancy engineering can effectively ameliorate the electronic structure and boost the ion transmission process without devastating the primitive spinel structure.

To directionally design LiMn_2O_4 materials at macroscopical and microcosmic levels, the utilization of self-sacrificial templates is a viable tactic. Metal-organic frameworks (MOFs) are a type of porous organic-inorganic hybrid crystalline materials that have been widely employed as templates for energy material fabrication owing to their intrinsic porosity and compositional/morphological multiformity.^[17–20] The MOF-templated strategy can impart spinel materials with excellent controllability in particle size, morphology, crystallinity degree, and oxygen defect concentration,^[21,22] which is suitable for the directional preparation and multiscale design of these materials. Despite the predominant advantages of oxygen vacancies in LiMn_2O_4 , the negative effects brought by oxygen vacancies are inescapable. The presence of oxygen defects may trigger Mn migration, increase the ratio of Mn^{3+} , and hence exacerbate Mn^{2+} dissolution and capacity decay.^[23,24] Therefore, countermeasures are necessary for the prohibition of Mn loss in the oxygen-deficient LiMn_2O_4 to exert the advantages of oxygen defects. To mitigate the surface Mn dissolution, the surface coating strategy has drawn specific attention, during which protective layers like metal oxides were adopted to restrain Mn ions and maintain the spinel structure.^[16,25,26] Surficial/interfacial kinetics can significantly impact the electrochemical behaviors at different operating conditions, so the rational selection of coating materials is vital to the simultaneous preservation of lithium storage capacity and structural integrity. With this aim, ionically/electronically conductive surface coatings are feasible for inhibiting structural degradation and synchronously warranting unimpeded ion/charge transfer.^[27,28] Zeolitic imidazolate framework (ZIF) glasses are capable of ensuring the homogeneous lithium ion flux and buffering the structural deterioration, which can be accredited to their grain boundary-free and isotropic properties related to the partial breakage of metal-nitrogen bonds as well as considerable electrical conductivity.^[29–31] Fascinating physicochemical properties of glassy ZIFs compared with crystalline ZIFs enable them to be ideal selective ion transport layers and elastic buffers for electrode materials.^[32,33] Therefore, the ZIF glass layer can not only be used to enhance the structural robustness of LIB anodes but also be applied as a shield to thwart cation loss in LIB cathodes.

Motivated by the above research progress, we propose a novel strategy to integrate MOF-templated synthetic route and ZIF glass coating strategy to controllably synthesize and multidimensionally modify spinel LiMn_2O_4 cathodes. Mn-MOFs with 1,4-dicarboxybenzene, 1,3,5-benzenetricarboxylic acid, and pyromellitic acid as bridging organic ligands (denoted as Mn-BDC, Mn-BTC, and Mn-PTC, respectively) are adopted as self-sacrificial templates to design a series of spinel LiMn_2O_4 materials with different structural properties and oxygen vacancy levels (abbrevi-

ated as LMO-1, LMO-2, LMO-3, accordingly). Bestowed by the superior crystal growth and higher oxygen vacancy concentration, LMO-1 outperforms its counterparts in reversible capacity and rate capability. Both experimental and theoretical investigations substantiate the effective modulation by MOF templates and the positive effects of oxygen defects in lithium storage. Based on these findings, considering the intensified Jahn-Teller distortion triggered by the increasing Mn^{3+} proportion with the presence of oxygen defects, the glassy Zn-ZIF-62 layer (abbreviated as Zn-ZIF-62-g) is utilized as a protective layer for LMO-1 (denoted as LMO-1-g). The Zn-ZIF-62 glass shield not only enables unimpeded ion/charge transfer but also alleviates the Mn^{2+} dissolution upon cycling, thereby rendering LMO-1-g a longevous cathode material in both LIB half cell (120.6 mAh g⁻¹ with a capacity retention of 88% at 1 C for 500 cycles; 83.7 mAh g⁻¹ with a capacity retention of 82% at 5 C for 2500 cycles) and full cell (120.9 and 85.5 mAh g⁻¹ for 150 cycles at 1 C and 2 C, respectively). This work successfully balances the merits of oxygen vacancy engineering and Zn-ZIF-62 glass coating and hence offers valuable insights into the multiscale design of spinel materials.

2. Results and Discussion

The self-sacrificial templated fabrication of LiMn_2O_4 cathode materials and the mechanisms are illustrated in Figure S1 (Supporting Information). Initially, Mn-MOF precursors (Mn-BDC, Mn-BTC, and Mn-PTC) were solvothermally synthesized and employed as self-sacrificial templates to design $\text{Mn}_2\text{O}_3/\text{C}$ intermediates (denoted as MOC-1, MOC-2, and MOC-3, accordingly) and LiMn_2O_4 products (LMO-1, LMO-2, and LMO-3). The powder X-ray diffraction (PXRD) patterns of Mn-MOFs indicate their high crystallinity degree and phase purity (Figure S2a, Supporting Information). According to the thermogravimetric analysis (TGA) result under the nitrogen atmosphere (Figure S2b, Supporting Information), the decomposition temperatures of Mn-MOFs are 500–650 °C, based on which a calcination temperature of 700 °C was applied to obtain MOC composites.^[34] To verify the successful synthesis of MOC composites, the XRD measurement was adopted to identify the crystallographic feature. As displayed in Figure S3a (Supporting Information), the characteristic peaks centred at 23.1°, 32.9°, 38.2°, 45.1°, 49.3°, 55.1°, and 65.7° are consistent with the standard card of cubic Mn_2O_3 (PDF #41-1442).^[35,36] The reductive calcination atmosphere enabled the retention of carbon skeletons in MOC composites. The carbon content in MOC-1, MOC-2, and MOC-3 are 36%, 26%, and 18%, respectively, as elucidated by TGA curves (Figure S3b, Supporting Information). Subsequently, LiMn_2O_4 products were prepared by a high-temperature sintering process at 800 °C to warrant the high crystallinity degree, by which the meticulous control from morphological/atomic levels can be realized.^[21,22] The increasing steric hindrance of organic ligands can result in decreasing cluster connectivity, thereby tapering the crystal growth, strengthening the nucleation process, and exacerbating the particle agglomeration.^[37] It's worth noting that the MOF-templated strategy can introduce oxygen defects and modulate their content, which can be attributed to the reductive atmosphere created by the organic ligands and the different amount of vacancy-acceptable sites endowed by the size/morphology effects.^[22,38,39] The lower oxygen defect level caused by the diminishing

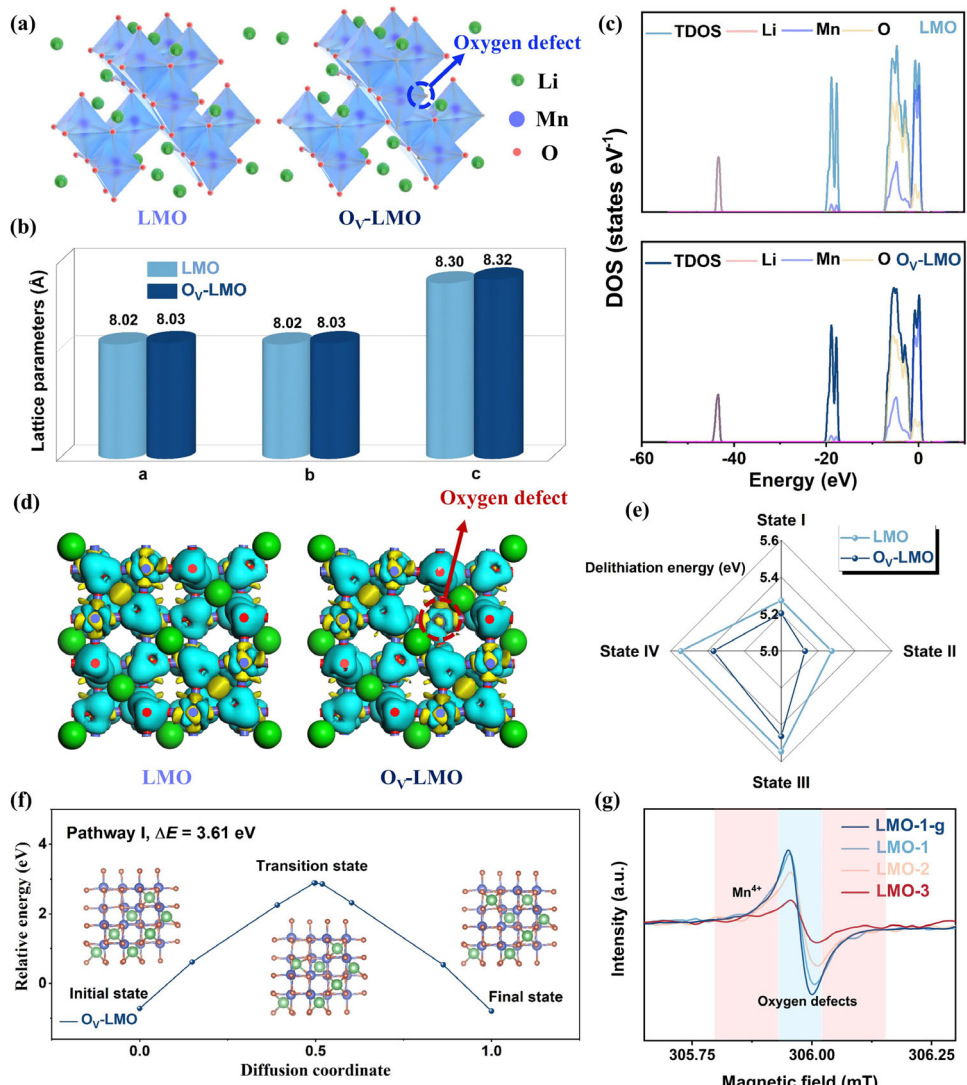


Figure 1. a) The optimized model, b) lattice parameters, c) DOS curves at the original state, d) front views of 3D differential charge density distributions, and e) calculated delithiation energies to states I–IV for LMO and O_v-LMO. f) Pathway I for Li⁺ migration in O_v-LMO and the corresponding energy barrier curve. g) The EPR curves for LMO-1-g, LMO-1, LMO-2, and LMO-3.

vacancy-acceptable sites and smaller specific surface area triggers the increasing <100> crystal orientation, thereby resulting in the formation of typical LiMn₂O₄ octahedrons.^[14] On the contrary, the higher oxygen defect concentration induces slower crystal growth along <100> and faster crystal growth along <111>, leading to the formation of truncated LiMn₂O₄ octahedrons. Hence, the MOF-mediated synthesis process plays a part in the modulation of the particle growth and oxygen defect level of LiMn₂O₄ products.

To unravel the effects of oxygen defects on lithium storage behaviors of LiMn₂O₄, density functional theory (DFT) calculation was implemented with the Materials Studio CASTEP program.^[40,41] The models of LiMn₂O₄ and oxygen-deficient LiMn₂O₄ with typical MnO₆ octahedral units were established and optimized (nominated as LMO and O_v-LMO, respectively), as displayed in **Figure 1a**. The optimized O_v-LMO model delivers larger lattice parameters compared with the primitive

LMO (Figure 1b) due to the lattice expansion induced by oxygen defects.^[16,42] Apart from the crystalline configuration, the electronic structure affected by the oxygen vacancies was also investigated. The presence of oxygen defects enables the hybridization of split peaks in the density of states (DOS) profiles at original/delithiated states of O_v-LMO (Figure 1c; Figure S4, Supporting Information), thereby confirming the local charge redistribution.^[43] The denser electron cloud around the Fermi level is also identifiable in the DOS profiles with the existence of oxygen defects, which can favor the electron transfer process and hence enhance the electronic conductivity.^[44] The 3D differential charge density distributions of LMO and O_v-LMO further substantiate the above inference, where lopsided charge distribution appears around the oxygen defect site (Figure 1d; Figure S5, Supporting Information). This can facilitate the formation of the local built-in electric field and boost the Li⁺ mobility,^[45] thereby expediting electrochemical kinetics. When delithiated to

different states (Figure S6, Supporting Information), the lower delithiation energies of O_v-LMO compared with LMO (Figure 1e) further support the formation of oxygen defect-induced positive charge domains facilitating lithium extraction.^[45] Considering the dominant role of Li⁺ mobility in lithium storage, the lithium vacancy migration energy barriers were also evaluated. Figure 1f presents an energy barrier of 3.61 eV along the pathway I in O_v-LMO, which is significantly lower than the one (3.92 eV) in LMO (Figure S7a, Supporting Information). Along pathway II, O_v-LMO also outperformed LMO (Figure S7b,c, Supporting Information) in lithium diffusivity with a smaller energy barrier of 0.85 eV. These theoretical findings jointly elucidate the modified crystal/electronic configuration, enhanced electronic conductivity, and boosted lithium diffusion kinetics in the oxygen-deficient LiMn₂O₄.

As mentioned earlier, the MOF-templated strategy can effectively manipulate the concentration of oxygen vacancies in the LiMn₂O₄ lattice. The electron paramagnetic resonance (EPR) test was conducted to compare the oxygen vacancy level of MOF-templated LiMn₂O₄ products. As depicted in Figure 1g, the sharp signals at $g = 2.003$ can be attributed to oxygen defects, while the broad Lorentzian lines at $g = 1.998$ are associated with the unpaired electrons of Mn⁴⁺.^[46] The higher peak intensity of LMO-1 at $g = 2.003$ indicates its higher oxygen defect concentration compared with its counterparts, which can be ascribed to the smaller particle size, larger specific surface area, and more affluent vacancy-acceptable sites imparted by the rational selection of self-sacrificial templates.^[38,39] Although the benefits of oxygen-deficient traits are widely admitted, the increased Mn³⁺ content and Jahn-Teller distortion issue in oxygen-deficient spinel materials are inevitable.^[24,47] Inspired by these, the Zn-ZIF-62 layer was grown on LMO-1 (LMO-1-Z) by the solvothermal approach (≈ 5 wt% Zn-ZIF-62), after which the melt-quenching process was executed to form a Zn-ZIF-62 glass protective layer (LMO-1-g),^[48] as portrayed in Figure 2a. The EPR result of LMO-1-g suggests that the introduction of the Zn-ZIF-62 coating layer hardly affects the oxygen-deficient nature of LMO-1, thereby indicating the possibility and rationality of combining oxygen vacancy engineering and Zn-ZIF-62 glass coating. According to the TGA curve of Zn-ZIF-62 (Figure S8a, Supporting Information), the decomposition temperature (T_d) of Zn-ZIF-62 is ≈ 550 °C. By the differential scanning calorimetry (DSC) scans (Figure S8b, Supporting Information), the glass transition temperature (T_g) and the melting point (T_m) were determined as 296 and 376 °C, respectively.^[49] Apparently, the T_m lower than T_d is a premise for the formation of MOF glass rather than porous carbon during the thermal treatment process.^[50] The high T_g/T_m value (≈ 0.79) of Zn-ZIF-62 also reveals its higher glass-forming ability compared with most MOFs (<2/3),^[51] further warranting the successful glass transition of crystal Zn-ZIF-62. These results can be valuable information for temperature control during the melt-quenching process. The LMO-1-Z was first heated up to 450 °C with a ramping rate of 20 °C min⁻¹ and then kept for 10 min, after which the sample was abruptly quenched back to room temperature. To substantiate the successful vitrification by this melt-quenching method, Fourier transform infrared (FT-IR) spectroscopy and Raman measurement were performed. As displayed in Figure S9a (Supporting Information), the typical chemical bond connection remains unchanged (i.e., the C–N stretching mode of imidazolate ligands),

where the signal of C=O stretching vibration located at 1715 cm⁻¹ related to the residual solvent disappears after the vitrification process.^[31] The Raman spectra also testify to the C–N stretching mode (ca. 1281 and 1181 cm⁻¹) of both Zn-ZIF-62 and Zn-ZIF-62-g (Figure S9b, Supporting Information). The emerging wide-band around the C–N stretching mode can be observed in the Zn-ZIF-62-g sample, which can be accredited to the suppression of long-range ordered structure and the formation of new chemical bonds during the liquid state at temperatures above T_m .^[49] Enlightened by these results, it can be assumed that atomic rearrangement occurs in Zn-ZIF-62-g accompanied by the formation of short-range ordered and long-range disordered structures.

The structural variation caused by vitrification can also be identified by the XRD technique. The XRD pattern of Zn-ZIF-62 is well in line with the simulated result, while the Bragg peaks vanish in the XRD pattern of Zn-ZIF-62 glass with the emergence of broad peaks (Figure S10a, Supporting Information), thereby illuminating the destruction of dense crystalline structure and the formation of glassy phase.^[29,52] The characteristic peaks of minority Zn-ZIF-62 and majority cubic LiMn₂O₄ are available in the XRD pattern of LMO-1-Z (Figure 2b), preliminarily verifying the successful growth of Zn-ZIF-62 on LMO-1. After the melt-quenching process, the LMO-1-g sample shows no characteristic peak of Zn-ZIF-62, whose XRD pattern aligns with the ones of MOF-derived samples (LMO-1, LMO-2, and LMO-3) and the solid-state fabricated sample (LMO-S), as illustrated in Figure 2c. All these samples bear the same crystallographic texture of cubic spinel LiMn₂O₄ with the $F\bar{d}3m$ space group,^[53] indicating satisfactory phase purity and high crystallinity degree. As the oxygen vacancy level increases, there is a slight shift to lower diffraction angles of the (111) facets in XRD patterns. This is attributed to the lattice expansion related to shared O atoms brought by oxygen vacancies.^[42,46] To further differentiate the atomic configuration influenced by MOF precursors, Rietveld refinements were conducted for MOF-derived LiMn₂O₄. All refined XRD patterns (Figure 2d; S10b-d, Supporting Information) suggest a good agreement between the experimental and calculated results. The lower oxygen occupations of LMO-1-g and LMO-1 indicate their higher oxygen defect concentration, accompanied by the increase in lattice constants and cell volumes (Table S1, Supporting Information).^[54]

Raman spectroscopy was applied to unearth the chemical bonding in LMO-1-g, LMO-1, LMO-2, and LMO-3 (Figure 2e). The pronounced vibration peaks located at 625, 580, 485, and 370 cm⁻¹ are associated with the A_{1g}, T_{2g}(1), T_{2g}(2), and T_{2g}(3) modes of the symmetric stretching vibration in the MnO₆ octahedron.^[55,56] The asymmetric peak at 625 cm⁻¹ indicates the coexistence of [Mn⁴⁺–O₆] and [Mn³⁺–O₆] octahedrons.^[57] In addition, the relative peak intensity of the shoulder peak at 580 cm⁻¹ can reflect the content of Mn⁴⁺.^[22] The peak intensity ratios at 580 and 625 cm⁻¹ of LMO-1-g and LMO-1 are lower than the ones of LMO-2 and LMO-3 (Figure S11, Supporting Information), revealing their superiority in Mn³⁺ content and oxygen defect concentration. Notably, the additional features at 315 and 290 cm⁻¹ of LMO-1-g are assigned to the Zn–N stretching mode,^[49] elucidating the existence of the ZIF glass coating layer. The FT-IR results also embody differences in chemical bonding caused by ZIF glass coating (Figure 2f). The absorption peaks at 480–540, 580–640, and 850–1150 cm⁻¹ are correlated to the Mn³⁺–O, Mn⁴⁺–O, and

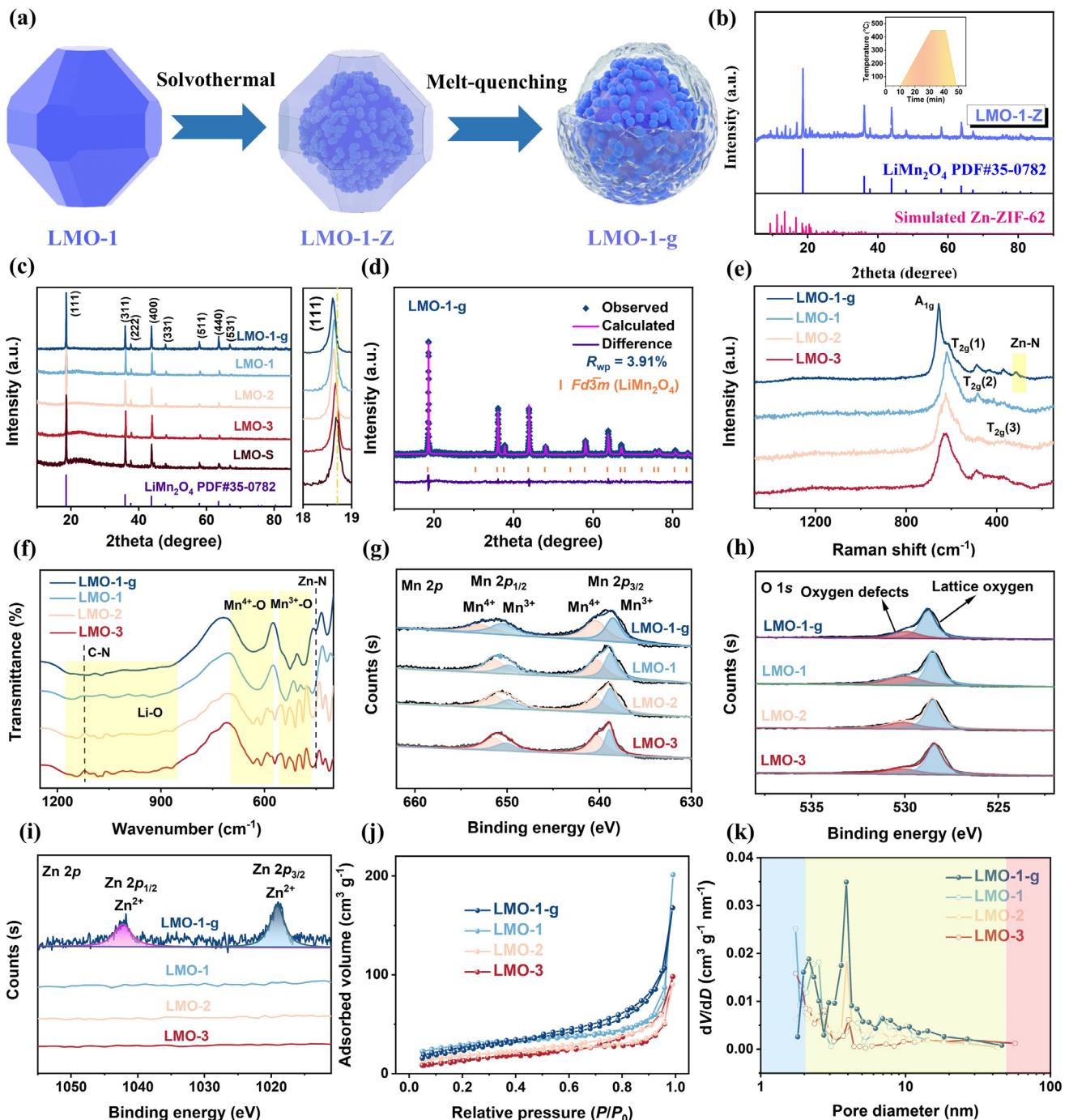


Figure 2. a) The schematic illustration for the fabrication of LMO-1-g. b) the XRD pattern for LMO-1-Z (inset: the temperature curve for the melt-quenching process). c) The XRD patterns for LMO-1-g, LMO-1, LMO-2, LMO-3, and LMO-S. d) The Rietveld refinement of LMO-1-g. e) The Raman spectra, f) FT-IR curves, g) Mn 2p, h) O 1s, and i) Zn 2p high-resolution XPS spectra, j) nitrogen adsorption-desorption isotherms, and k) corresponding pore distribution curves for LMO-1-g, LMO-1, LMO-2, and LMO-3.

Li–O stretching vibration, respectively.^[58,59] Meanwhile, the FT-IR curve of LMO-1-g exhibits different traits compared with the counterparts without ZIF glass coating, including inconspicuous absorption peaks centered at 450 and 1120 cm⁻¹, corresponding to Zn–N and C–N stretching modes, respectively.^[31,48,49]

For the in-depth analysis of elements and chemical states, X-ray photoelectron spectroscopy (XPS) was adopted. Figures S12 and S13 (Supporting Information) illustrate the coexistence of Zn, C, and N in Zn-ZIF-62 and Zn-ZIF-62-g and verify the invariant bonding environment during the melt-quenching process.^[48] The survey-scan XPS spectra (Figure S14, Supporting

Information) also reflect the similar chemical composition of LMO-1-g, LMO-1, LMO-2, and LMO-3, while the presence of Zn 2p (1011–1055 eV) and N 1s (\approx 396 eV) in LMO-1-g originates from the ZIF-62 glass layer. The characteristic peaks at 46.7 eV in the high-resolution Li 1s XPS spectra (Figure S15a, Supporting Information) illustrate the successful sintering lithiation.^[60] The high-resolution N 1s XPS spectra (Figure S15b, Supporting Information) highlight the characteristic peak at 397.3 eV of LMO-1-g, which is assignable to the presence of imidazole ligands.^[48,52] To identify the chemical states of Mn and O, core-level Mn 2p and O 1s spectra were deconvoluted. As delivered in Figure 2g, the oxidation states of these samples include 3+ and 4+, based on which the Mn³⁺ concentrations of LMO-1-g, LMO-1, LMO-2, and LMO-3 can be calculated as 53.2%, 53%, 52.1%, and 50.5%, respectively (Figure S16a, Supporting Information).^[12,22,25,60] Apart from Mn³⁺ contents, oxygen defects can also be reflected by the deconvoluted peaks in the high-resolution O 1s spectra (Figure 2h). The characteristic peaks at 529 and 531 eV are correlated to the lattice oxygens and oxygen defects, respectively.^[15,16] Notably, LMO-1-g and LMO-1 exhibited higher relative peak intensities at 531 eV (the lattice oxygen peak intensities at 529 eV as the reference of 100%), thereby corroborating their higher oxygen defect contents,^[42,46] as summarised in Figure S16b (Supporting Information). In addition, the high-resolution Zn 2p spectra (Figure 2i) pronouncedly differentiate the chemical composition of LMO-1-g and other MOF-templated counterparts with two deconvoluted peaks at 1042 and 1019 eV. This indicates the existence of Zn with a chemical state of 2+ in LMO-1-g due to the successful ZIF glass coating.^[48,61]

The pore structures of these materials were studied by the Brunauer–Emmett–Teller (BET) measurement. As demonstrated in Figure 2j, all MOF-derived LiMn₂O₄ samples feature type III nitrogen adsorption/desorption curves with the hysteresis phenomenon at high relative pressures, which is ascribed to the well-retained porous structures from Mn-MOF precursors.^[21] The specific surface areas of LMO-1-g, LMO-1, LMO-2, and LMO-3 are 97.7, 100.1, 63.9, and 54.9 m² g⁻¹, respectively. Furthermore, the micro-mesoporous feature can be jointly observed in these samples (Figure 2k). The large specific surface area and highly developed porosity are endowed by the Mn-MOF precursors, which favor electrolyte infiltration and ion diffusion.^[11,62] The MOF-mediated synthesis method also enables the meticulous control of specific surface areas relying on the competition between crystallization and nucleation, during which the smaller linker steric hindrance can increase the cluster connectivity and hence facilitate the crystallization process and ameliorate particle growth.^[37] Consequently, LMO-1-g and LMO-1 possess larger specific surface areas and higher porosity due to the proper selection of organic ligands. It's worth noting that the vitrification process can hardly taper the specific surface area of Zn-ZIF-62 (Figure S17a, Supporting Information), during which the porous nature is also perfectly inherited (Figure S17b, Supporting Information).^[31,50] This warrants the unimpeded ion transmission aisles and the undisturbed electrode/electrolyte contact after ZIF glass modification.

The glass transition process destructs the ordered structure of Zn-ZIF-62 and results in the vanishing grain boundaries, ensuring the unobstructed Li⁺ migration after Zn-ZIF-62 glass coating of LMO-1,^[29,32] as illustrated in Figure 3a. To explain

the distinct differences in physical properties of crystal/glassy Zn-ZIF-62 (Figure S18a, Supporting Information) and LiMn₂O₄ materials with/without ZIF-62 coating (Figure S18b, Supporting Information), optical properties before and after vitrification were studied by the polarised light microscopy. As expected, the optical isotropy of Zn-ZIF-62 glass (Figure 3b) and the optical anisotropy of crystal Zn-ZIF-62 (Figure 3c) were confirmed, indicating the remarkable optical variations caused by the vitrification process.^[52,63] The scanning electron microscopy (SEM) images of Zn-ZIF-62 (Figure S19a,b, Supporting Information) and Zn-ZIF-62-g (Figure S19c,d, Supporting Information) also reveal significantly different morphological properties after vitrification, where the rougher surface of Zn-ZIF-62-g and the change in particle shape can be attributed to the appreciable flow in the liquid Zn-ZIF-62.^[63,64] After the carbonization process, the panoramic morphologies of the Mn-MOF precursors can be found in the MOC intermediates (Figure S20, Supporting Information), indicating the undamaged carbon skeletons by pyrolysis under the inert atmosphere.^[34] The high-temperature sintering procedure enables the solid-state conversion to LiMn₂O₄ products, during which the particle growth can be modulated by the organic ligand species from molecular and atomic levels.^[21] Truncated octahedral structures are available in SEM images of LMO-1 (Figure 3d), LMO-2 (Figure S21a, Supporting Information), and LMO-3 (Figure S21b, Supporting Information). The truncated octahedral feature in LMO-1 is more distinct compared with LMO-2 and LMO-3, which is associated with the higher oxygen vacancy level. This structural evolution from octahedral to truncated octahedral is accredited to the variations in surface crystallographic orientations triggered by oxygen defects, accompanied by the appearance of corner (001) planes.^[14,47] LMO-1-Z (Figure S21c, Supporting Information) and LMO-1-g (Figure 3e) presented similar truncated octahedral structures to LMO-1 with pronounced changes in surficial properties, indicating the successful in situ growth and vitrification of Zn-ZIF-62.^[64] The particle sizes of LMO-1-g, LMO-1-Z, LMO-1, LMO-2, and LMO-3 were also statistically recorded in Figure 3f. Among them, LMO-1-g, LMO-1-Z, and LMO-1 delivered smaller average particle diameters (<250 nm) compared with LMO-2 and LMO-3. This can be attributed to the alleviated secondary growth of particles originating from the stronger crystallization orientations imparted by the BDC ligands with lower steric hindrance.^[22,37]

The crystal structures were further explored using transmission electron microscopy (TEM) characterization. The TEM images of LMO-1 (Figure S22a, Supporting Information), LMO-2 (Figure S22b, Supporting Information), and LMO-3 (Figure S22c, Supporting Information) are consistent with SEM results in morphologies and particle sizes. The coating layers of LMO-1-Z (Figure S22d, Supporting Information) and LMO-1-g (Figure 3g) can also be roughly visualized in TEM images, where the thickness of the Zn-ZIF-62 glass layer is \approx 7 nm. The high-resolution TEM (HRTEM) images are powerful tools to identify the lattice fringes and distinguish the crystalline/non-crystalline phases. As illustrated in Figure S22e–g (Supporting Information), the distinct lattice fringes with a lattice spacing of 0.48 nm are in line with the interplanar spacing of the (111) plane in the spinel lithium manganate phase.^[53,65] As for LMO-1-Z (Figure S22h, Supporting Information), crystallographic features of both Zn-ZIF-62 and LiMn₂O₄ are detectable. Lattice fringes of 0.35 nm are

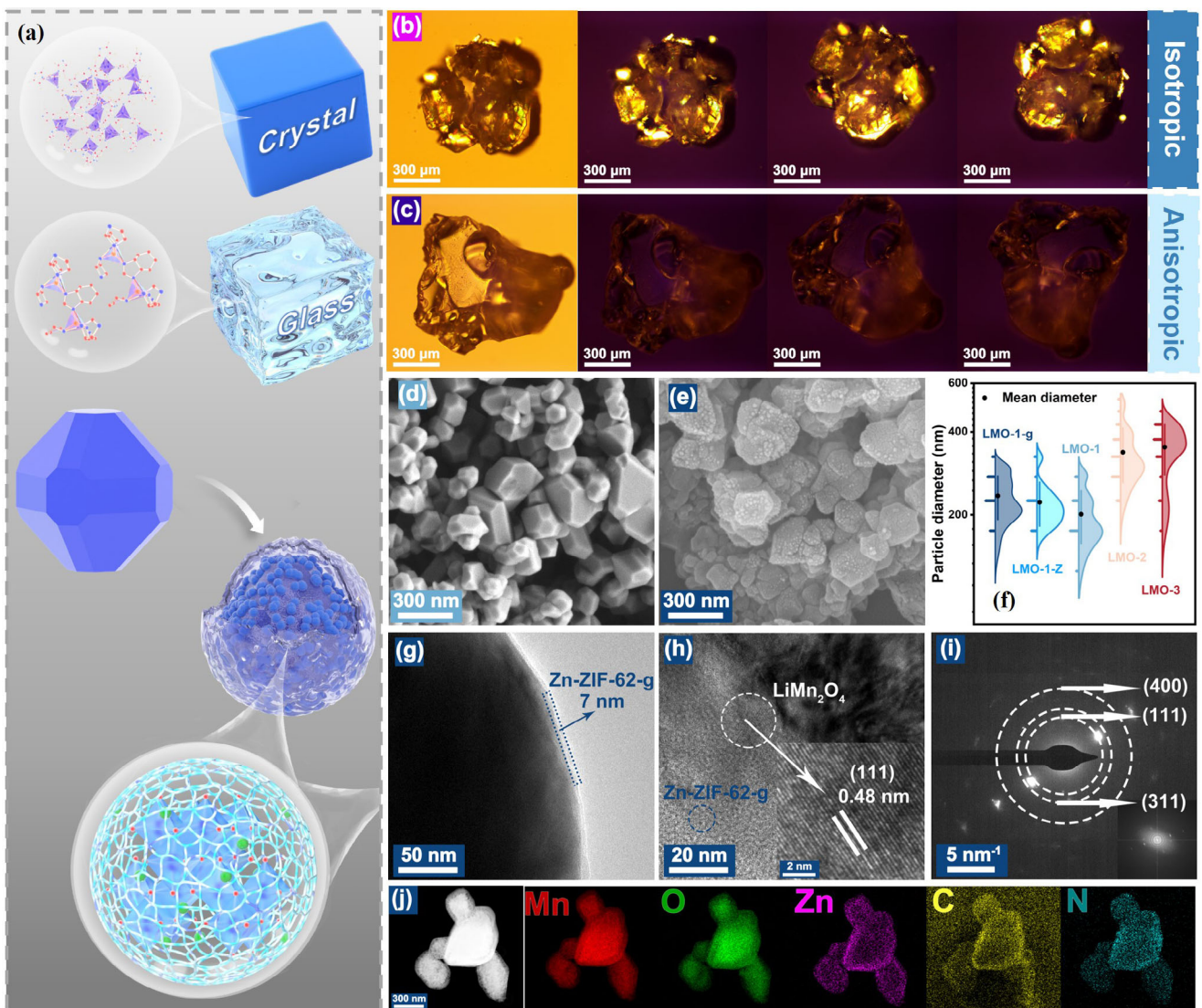


Figure 3. a) The schematic illustration of the structure evolution during the vitrification process. The optical images under parallel-polarized light (left) and crossed-polarized light for b) Zn-ZIF-62 and c) Zn-ZIF-62-g. The SEM images of d) LMO-1 and e) LMO-1-g. f) The statistical particle diameters of LMO-1-g, LMO-1-Z, LMO-1, LMO-2, and LMO-3. g) The TEM image, h) the HRTEM image, i) the SAED image (inset: FFT image), and j) HAADF-STEM images and corresponding element mappings for LMO-1-g.

available on the surface of LMO-1-Z, which are associated with the ordered crystal structure of the Zn-ZIF-62 layer.^[52] The melt-quenching treatment enables the transformation of Zn-ZIF-62 from crystal to glassy states, during which the ordered structure is devastated and the crystal configuration of the LiMn₂O₄ bulk remains unaffected (Figure 3h). Additionally, the selected area electron diffraction (SAED) patterns and fast Fourier transform (FFT) images (Figure 3i; Figure S22i-l, Supporting Information) intuitively illustrate the polycrystalline structure of spinel lithium manganate, in which electron diffraction rings indexed to (111), (311), and (400) planes of the $F\bar{d}3m$ spinel phase are visible,^[16,42] thereby revealing the satisfactory phase purity and high crystallinity degree. To examine the phase homogeneity of these materials, the high-angle annular dark-field scanning TEM (HAADF-STEM) images and corresponding element map-

pings are disclosed in Figure 3j, Figures S23, and S24 (Supporting Information). All these results reveal the uniform distribution of Mn and O related to the successful fabrication of LiMn₂O₄ bulk materials. The differences in the chemical composition of LMO-1-Z and LMO-1-g can also be unraveled by the additional traits of Zn, C, and N elements. These elements evenly distribute over the surface, thereby illustrating the uniform growth of crystal/glassy Zn-ZIF-62 on LMO-1. The synchrotron X-ray micro-computed tomography (micro-CT) is a useful tool to evaluate structural integrity and continuity (Figure S25, Supporting Information), by which a dense structure without significant fracturing can be identified in Zn-ZIF-62 after the melt-quenching process, thereby implying the possibility of forming a continuous glassy protective shell.^[66] To further support the uniform surface coating and evaluate the thickness of the glassy Zn-ZIF-62 layer,

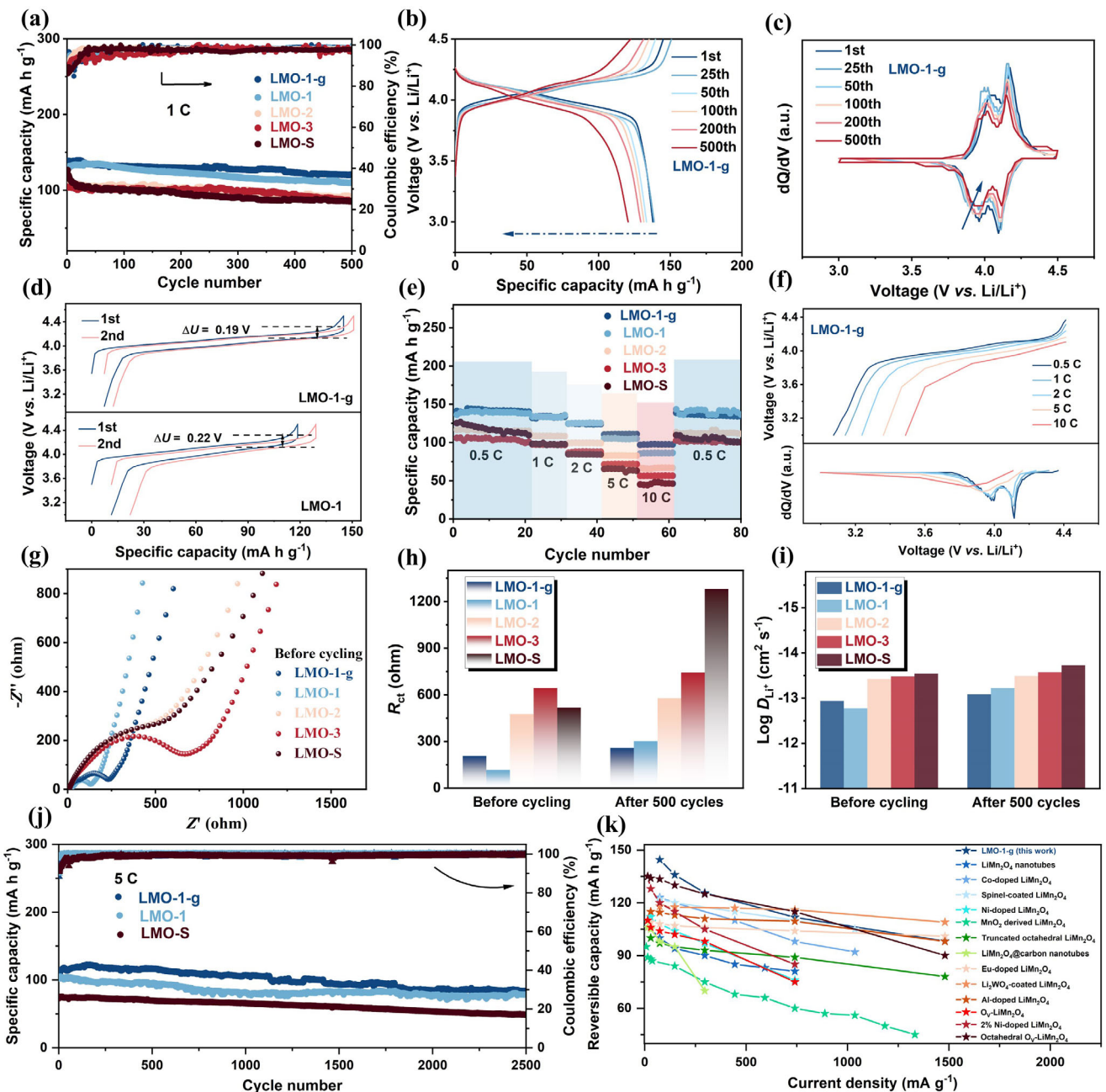


Figure 4. a) The cycling performance of LMO-1-g, LMO-1, LMO-2, LMO-3, and LMO-S at 1 C. b) The GCD and c) dQ/dV curves at 1 C of LMO-1-g. d) The voltage hysteresis plots at 1 C of LMO-1-g and LMO-1. e) The rate capability of LMO-1-g, LMO-1, LMO-2, LMO-3, and LMO-S. f) The discharge curves and corresponding dQ/dV curves of LMO-1-g from 0.5 to 10 C. g) The Nyquist plots before cycling, h) the fitted R_{ct} values, and i) the calculated D_{Li^+} values of LMO-1-g, LMO-1, LMO-2, LMO-3, and LMO-S. j) The long-term cycling performance of LMO-1-g, LMO-1, and LMO-S at 5 C. k) The performance comparison of various LiMn₂O₄ cathode materials.^[6,8,12,14–16,27,43,55,56,60,65,68]

the Ar⁺ etching XPS technique was employed. As illuminated in Figure S26 (Supporting Information), the Zn 2p and N 1s peaks entirely vanish after Ar⁺ etching down to 10 nm, which is consistent with the TEM result.

Succeeding the material characterisations, the electrochemical behaviours of these self-sacrificial templated LiMn₂O₄ cathodes were explored in detail to excavate the structure-activity correlation. During the galvanostatic measurement, LMO-1-g

and LMO-1 outperformed other MOF-derived and conventionally synthesized counterparts in reversible capacity and cyclability (Figure 4a) due to their optimized morphological features, higher oxygen vacancy level, and stronger crystalline orientation. This unambiguously manifests the role of MOF templates as structure-directing agents to enhance the electrochemical performance of spinel materials.^[67] After 500 cycles at 1 C, LMO-1-g exerted a remarkable reversible capacity of 120.6 mAh g⁻¹

with a capacity retention of 88%, surpassing the one of LMO-1 (110.9 mAh g⁻¹; 85% retention), as illustrated in Figure S27 (Supporting Information). This preliminarily illustrates the mitigated capacity attenuation induced by the ZIF-62 coating layer. In the galvanostatic charge/discharge (GCD) curves disclosed in Figure 4b and Figure S28 (Supporting Information), typical voltage plateaus of the Mn⁴⁺/Mn³⁺ redox couple are available above 4 V.^[15] The excellent repeatability of GCD curves with the increasing cycling number also indicates the satisfactory cycling durability of LMO-1-g. Apart from the GCD curves, the inward contraction of the dQ/dV curves (Figure 4c; Figure S29, Supporting Information) represents the capacity degradation.^[12] Among these, the dQ/dV curves of LMO-1-g remain stable as the cycle number increases, while the ones of LMO-S show more palpable contraction, thereby embodying the advantages of the MOF-templated route and ZIF glass modification strategy in prolonging the lifespan of spinel materials.

The redox kinetics during the repetitive Li⁺ insertion/extraction were evaluated with voltage hysteresis plots. As illuminated in Figure 4d, the weakened voltage hysteresis of LMO-1-g compared with LMO-1 indicates the smaller polarisation, exalted reversibility, and boosted electrochemical kinetics induced by the ZIF-62 glass shield.^[54] The intensified voltage hysteresis of LMO-S unravels its sluggish redox kinetics and dissatisfying cycling stability (Figure S30, Supporting Information), corresponding to its inferior capacity retention compared with MOF-templated counterparts. The electrochemical inertness of the Zn-ZIF-62 glass layer can be validated by the dQ/dV curve (Figure S31a, Supporting Information) and the linear scan voltammetry (LSV) curve (Figure S31b, Supporting Information) at 3–4.5 V, during which no redox activity was provided by Zn-ZIF-62-g when investigated as a LIB cathode,^[25] thereby indicating the excellent stability of Zn-ZIF-62 glass when employed as the coating layer for LiMn₂O₄. The rate capability measurements were further executed to verify the electrochemical kinetics of these materials. Among them, LMO-1-g delivered fabulous reversible capacities at different current densities (144.5, 135.9, 125.6, 111.7, and 98.2 mAh g⁻¹ at 0.5, 1, 2, 5, and 10 C, respectively) and excellent capacity recovery (142.9 mAh g⁻¹) when the current density bounded back to 0.5 C (Figure 4e). It's noteworthy that LMO-1-g and LMO-1 displayed similar reversible capacities at 0.5 C, but LMO-1-g significantly outperformed LMO-1 when operated at elevated current densities. The negligible sacrifice in reversible capacity when cycled at low current densities is attributed to the introduction of the electrochemically inert glassy protective layer.^[16] Despite the capacity loss caused by the surface coating, the high-rate capacity of LMO-1-g was significantly enhanced owing to the higher electron/Li⁺ transport efficiency, stabilized surface structure, and mitigated Jahn-Teller distortion.^[68] The electrochemical impedance spectroscopy (EIS) results at different current densities were provided to support this assumption (Figure S32, Supporting Information), where LMO-1-g showed a similar impedance value compared with LMO-1 at 0.5 C but pronouncedly surpassed LMO-1 in electron/ion diffusivity at 10 C. Accordingly, the more significant plateaus and higher dQ/dV peak intensities at elevated current densities indicate superior reversibility of LMO-1-g in the rate capability test (Figure 4f; Figure S33, Supporting Information).^[54,60] The extraordinary

rate capacity is also propitious to the energy density (Figure S34, Supporting Information), which is crucial for the practical application of spinel materials.

The electronic/ion conductivity during cycling was also investigated by EIS measurements. The Nyquist plots (Figure 4g; Figure S35a,b, Supporting Information) profoundly feature two semicircles at high and intermediate-frequency regions related to the surface film resistance (R_f) and the charge transfer resistance (R_{ct}), respectively, together with slope lines at the low-frequency region associated with Li⁺ diffusivity.^[61,67] The fitted results suggest that the fluctuation of electrolyte resistance (R_s) and R_f values are inconspicuous (Table S2, Supporting Information). The R_{ct} values can reflect the charge transfer velocity and are instrumental to the electrochemical kinetics.^[69] Figure 4h demonstrates the smaller R_{ct} values and faster charge transfer of LMO-1-g and LMO-1 during cycling, where LMO-1-g delivers a negligible increase in R_{ct} values after 500 cycles at 1 C, thereby revealing its buffered structural failure and prolonged lifespan. The lithium diffusion coefficient (D_{Li^+}) values were calculated by the formula of $D_{Li^+} = R^2 T^2 / 2A^2 n^4 F^4 c^2 \sigma^2$, where σ values were fitted by the $Z' - \omega^{-1/2}$ linear relationship (Figure 4i; Figure S35c,d, Supporting Information; details are given in the supporting information).^[42] LMO-1 and LMO-1-g exhibited smaller D_{Li^+} values compared with other samples, preliminarily testifying to the faster Li⁺ diffusion triggered by the reduced particle size and increased oxygen defect concentration. Noticeably, the D_{Li^+} value of LMO-1-g remained steady during cycling, which is accredited to the smooth lithium transport of the Zn-ZIF-62 glass layer endowed by the absence of grain boundary.^[29,32] This grain-boundary-free characteristic is favorable for the protection of the LiMn₂O₄ bulk without hampering Li⁺ transport, thereby immobilizing the spinel structure, expediting Li⁺ diffusion, and exerting stable reversible capacity. In contrast, the sluggish Li⁺ diffusion of crystal ZIF-62 results in the dissatisfactory reversible capacity (lower than 75 mAh g⁻¹) and cyclability of LMO-1-Z (Figure S36, Supporting Information).

To further verify the effective combination of oxygen defects and glassy Zn-ZIF-62 shield, the long-term cycling durability at elevated current densities/temperatures was evaluated. It's widely acknowledged that higher temperatures (especially ≥ 50 °C) can aggravate the Jahn-Teller distortion, resulting in the dissatisfactory high-temperature performance of LiMn₂O₄ that hinders its practical use.^[70] Motivated by this, the high-temperature performance measurement for the as-prepared LiMn₂O₄ materials was operated at different temperatures (40 and 60 °C) to examine the weather resistance in practice and endurance under extreme conditions. When cycled at the elevated temperature of 40 °C, LMO-1-g displayed an impressive reversible capacity of 98.5 mAh g⁻¹ with a capacity retention of 76% at 2 C over 1000 cycles (Figure S37a, Supporting Information). When the temperature was elevated to 60 °C (Figure S37b, Supporting Information), LMO-1-g presented significantly higher reversible capacity (128 mAh g⁻¹) and cyclability (72.8% retention over 800 cycles) compared with the conventionally synthesized sample, indicating its mitigated Jahn-Teller distortion and substantial adaptability under harsh operating conditions. As illuminated in Figure 4j, LMO-1-g outperformed LMO-1 and LMO-S in long-term cycling stability with an exceptional discharge capacity of 83.7 mAh g⁻¹ after 2500 cycles at 5 C (78.5 mAh g⁻¹

with a capacity retention of 77% for LMO-1; 48.7 mAh g⁻¹ with a capacity retention of 66% for LMO-S). Furthermore, LMO-1-g performed steadily at 10 C with an initial discharge capacity of 101.2 mAh g⁻¹, retaining 75% over 1000 cycles (Figure S38, Supporting Information). In contrast, LMO-1 without ZIF glass coating exerted inferior reversible capacity and cycling durability at 10 C (58.9 mAh g⁻¹ with a capacity retention of 68% after 1000 cycles) due to the blocked Li⁺/electron transfer aisles, adverse electrode/electrolyte contact, and intensified polarisation caused by surface structural deterioration.^[8,70] These dazzling properties overwhelm most of the previously reported spinel LiMn₂O₄ cathodes (Figure 4k), thereby validating the viability of oxygen vacancy engineering and selective glass protective layer confinement.

The electrochemical kinetics of as-prepared LiMn₂O₄ materials were further explored by cyclic voltammogram (CV) and galvanostatic intermittent titration technique (GITT) techniques. The CV curves at 0.2 mV s⁻¹ jointly feature two pairs of redox peaks located at ≈3.9 and ≈4.1 V (Figure 5a; Figures S39a, S40a, and S41a, Supporting Information), which are consistent with the GCD curves and can be ascribed to the two-step Mn⁴⁺/Mn³⁺ redox activities caused by the location of lithium ions on half of the tetrahedral 8a sites.^[28,56] The CV profiles after the first cycle almost overlap, indicating the satisfying reversibility of the lithium storage redox reaction. At the escalating scanning rates from 0.2 to 1.0 mV s⁻¹, the anodic peaks at 4.14 and 4.28 V as well as the cathodic peaks at 3.86 and 4.01 V (denoted as Peak 1, Peak 2, Peak 3, and Peak 4, respectively) can be detected (Figure 5b; Figures S39b, S40b, and S41b, Supporting Information). These can be utilized to quantitatively analyze the pseudocapacitive behaviors by formulas of $i = av^b$ and $i = k_1v + k_2v^{1/2}$ (details in the supporting information).^[34] The b values for Peaks 1–4 were fitted by the linear relationship between logarithms of the peak current and the scan rate ($\log i = b \log v + \log a$), where the fitted b values suggest the coexistence of both pseudocapacitive and diffusion-controlled processes (Figure 5c; Figures S39c, S40c, and S41c, Supporting Information).^[53] All samples presented increasing pseudocapacitive contribution ratios with the escalation of the scan rate (Figure 5d; Figures S39d, S40d, and S41d, Supporting Information). Among them, LMO-1-g and LMO-1 showed more pronounced pseudocapacitive contributions at different scan rates (Figure 5e), revealing their expedited lithium diffusion kinetics and superior rate performance induced by the increased oxygen vacancy concentration and optimized morphology.^[34,38] Moreover, the D_{Li}^+ values of different redox peaks were estimated by the linear relationship between i and $v^{1/2}$ (Figure S42, Supporting Information; calculation details are provided in the supporting information).^[16,54] LMO-1-g and LMO-1 delivered larger D_{Li}^+ values for Peaks 1–4, indicating their superior redox kinetics. These results also elucidate the undisturbed Li⁺ transport in LMO-1-g and reflect the remarkable ion conductivity of the Zn-ZIF-62 glass coating layer.

The GITT technique is another powerful tool to evaluate the lithium diffusion dynamics during the charge/discharge processes. The D_{Li}^+ values can be calculated according to the Fick's second law, where the equation of $D_{Li+} = \frac{4}{\pi r} \left(\frac{m_B V_M}{M_B A} \right)^2 \left(\frac{\Delta E_S}{\Delta E_r} \right)^2$ can be applied (Figure S43, Supporting Information).^[71] Correspondingly, the voltage responses at different states of charge/discharge

(Figure 5f; Figure S44, Supporting Information) reflect the overpotential related to the polarisation degree. It's widely acknowledged that the smaller overpotential indicates the smaller polarisation degree and kinetically favorable lithium diffusion.^[7] The calculated D_{Li}^+ values based on the full-step GITT titration profiles indicate faster lithium diffusion in LMO-1-g and LMO-1 (Figure 5g), matching well with the fitted results of CV measurements. Notably, the tendencies of the D_{Li}^+ curves manifest a similar lithium storage mechanism, where the abruptly declining D_{Li}^+ values around the voltage plateaus are correlated to the sluggish lithium diffusion caused by redox reactions.^[71] Aside from the D_{Li}^+ values, the reaction resistances (RR) upon charging/discharging were evaluated to illustrate the redox reaction kinetics (Figure 5h; details in the Supporting Information). The lower RR values validate the facilitated redox reaction dynamics of LMO-1-g and LMO-1, particularly at the high-voltage region.^[54] This accounts for the rapid Li⁺ diffusion and desirable rate capability of LMO-1-g and LMO-1. To expound the above results from the perspective of electronic configuration, the boosted Li⁺ diffusivity triggered by oxygen vacancies is schematically illustrated in Figure 5i. The presence of oxygen vacancies induces the lopsided charge distribution and local built-in electric fields, thereby expediting the Li⁺ migration by Coulomb forces.^[45] During the delithiation process, the positively charged area around oxygen vacancy sites results in positive electric forces against the neutral Li⁺ accumulation area, which accelerates Li⁺ extraction accompanied by the formation of a negatively charged region in the oxygen vacancy-free area. The negatively charged region exerts negative electric forces against the neutral oxygen vacancy-free area and boosts the lithiation process. Therefore, the oxygen-deficient feature is propitious to the boosted electrochemical kinetics due to the effective modulation of the electronic structure.

To validate the effectiveness of the Zn-ZIF-62 glass shield, *in situ* XRD measurements were implemented to monitor the crystallographic dynamics during the charge/discharge processes. The peak offsets of the (111), (311), and (200) Bragg peaks of LMO-1-g (Figure 6a) and LMO-1 (Figure S45, Supporting Information) during the lithium storage process are observable, correlating with the phase transformation upon charging/discharging.^[60,71] The offsets of characteristic peaks of LMO-1-g ($\Delta_{(111)} = 0.46^\circ$; $\Delta_{(311)} = 0.91^\circ$) are profoundly smaller than the ones of LMO-1 ($\Delta_{(111)} = 0.58^\circ$; $\Delta_{(311)} = 1.24^\circ$), thereby unraveling the mitigated volume fluctuation and strengthened structural robustness of LMO-1-g.^[12] Correspondingly, the lattice deformation during cycling was evaluated based on the *in situ* XRD results (Figure 6b). The variations in cell parameters during the lithiation/delithiation processes are 0.138 and 0.205 Å for LMO-1-g and LMO-1, respectively. According to these results, it can be observed that a smaller volume change was displayed by LMO-1-g upon the entire delithiation (27.73 and 40.77 Å³ for LMO-1-g and LMO-1, respectively). This suggests the more recoverable lattice deformation of LMO-1-g due to the inhibited Mn²⁺ dissolution and alleviated surface destruction induced by the Zn-ZIF-62 glass protective layer.^[71] As illustrated in Figure 6c, the structural distortion within MnO₆ octahedrons in LMO-1-g can be mitigated due to the successful confinement of Mn²⁺ ions and the superior structural reversibility. This assumption can be further substantiated by the *ex situ* XRD results (Figure S46, Supporting Information), where less heterophase

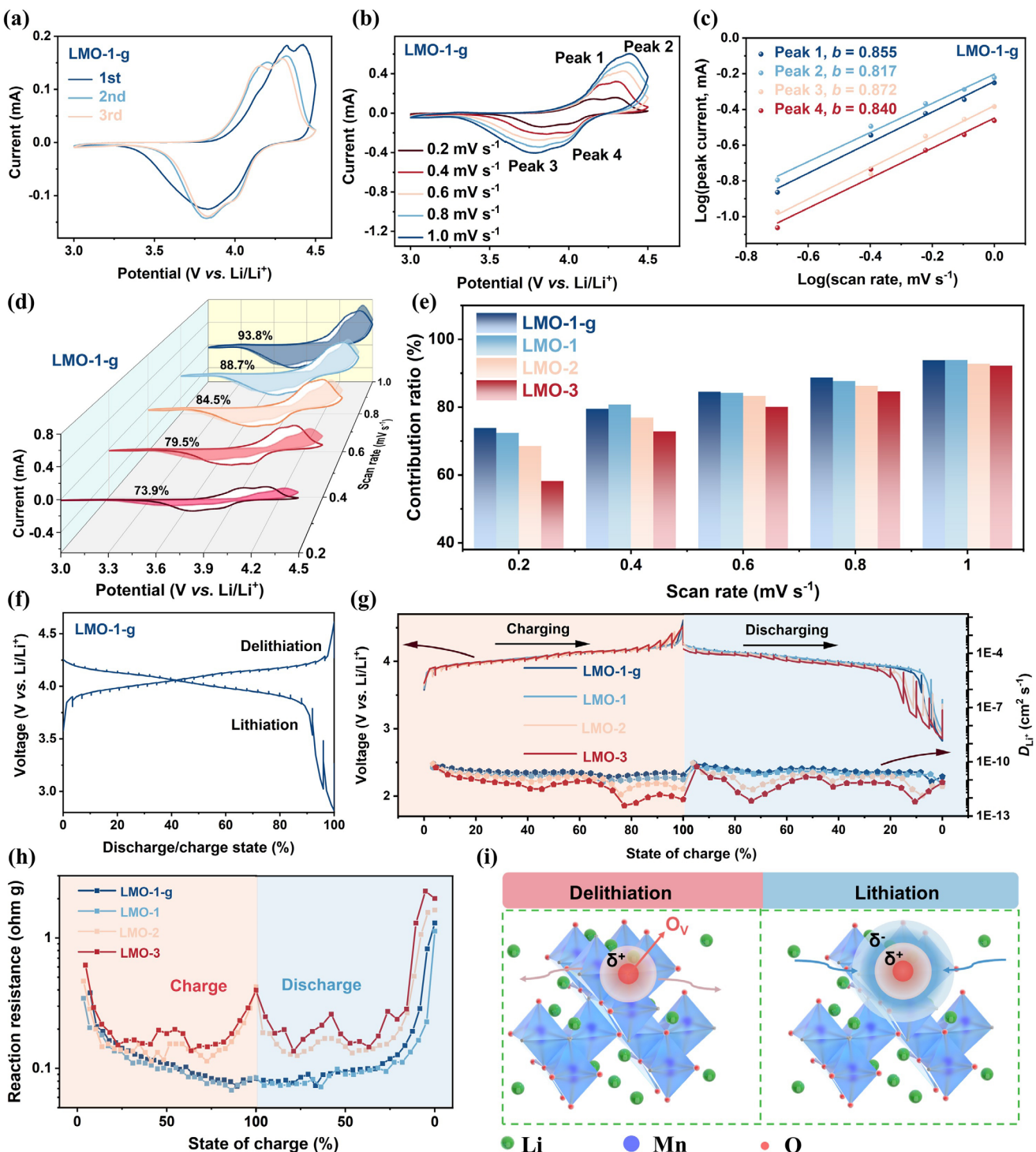


Figure 5. a) The CV curves at 0.2 mV s⁻¹ during the first 3 cycles, b) CV curves at different scan rates from 0.2 to 1.0 mV s⁻¹, c) the fitted *b* values for the main anodic and cathodic peaks, and d) the separation of the pseudocapacitive and diffusion-controlled currents for LMO-1-g. e) The pseudocapacitive contributions from 0.2 to 1.0 mV s⁻¹ for LMO-1-g, LMO-1, LMO-2, and LMO-3. f) The GITT charge/discharge curves for LMO-1-g. g) The full-step GITT titration profiles and the corresponding calculated D_{Li^+} values and h) the calculated RR values based on the GITT results for LMO-1-g, LMO-1, LMO-2, and LMO-3. i) The schematic illustration for the boosted lithium diffusion induced by oxygen vacancies.

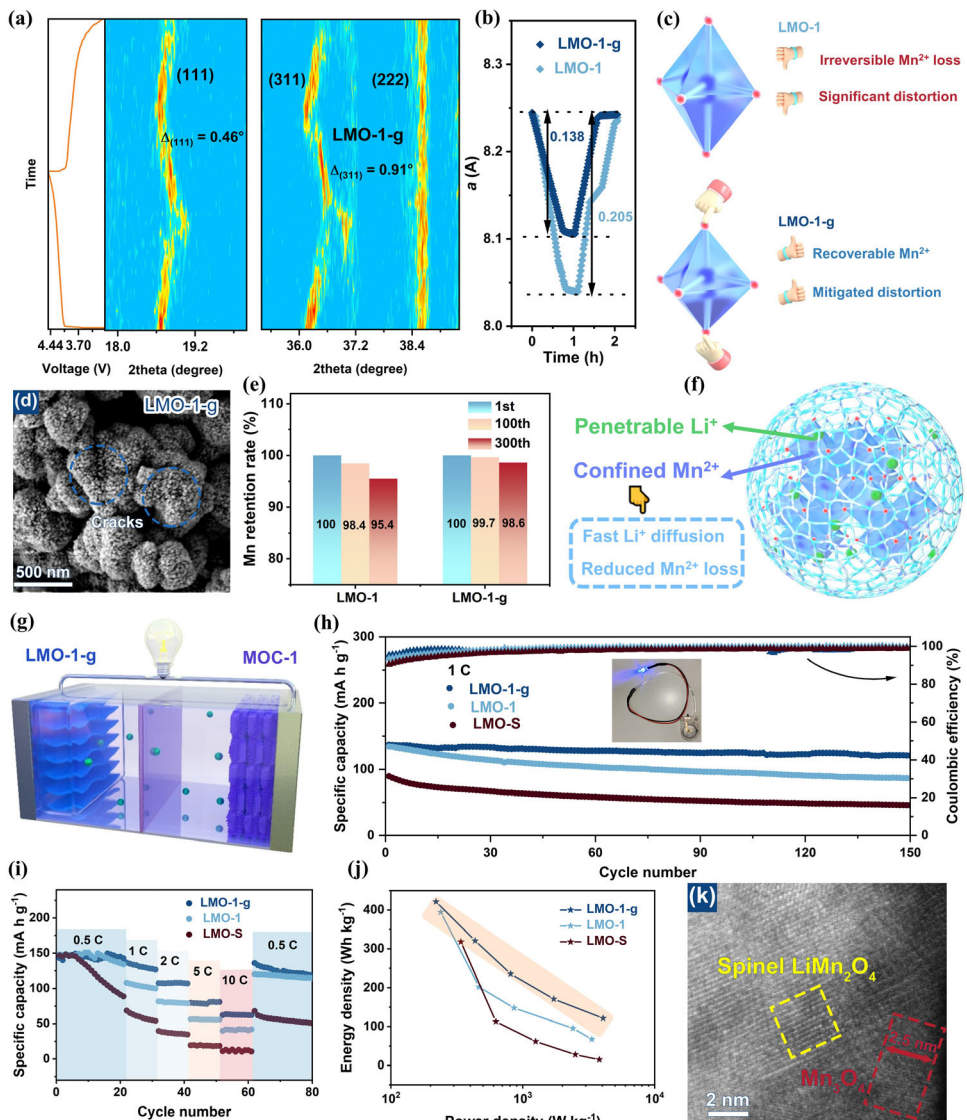


Figure 6. a) The in situ XRD patterns of LMO-1-g. b) The evolutions of the lattice parameter during the in situ XRD test for LMO-1-g and LMO-1. c) The schematic illustration of the inhibited Jahn-Teller distortion in the MnO₆ octahedrons and d) SEM image after 2500 cycles at 5 C for LMO-1-g. e) The Mn retention ratio during the cycling measurement at 1 C acquired by the ICP test for LMO-1-g and LMO-1. The schematic illustration of f) the ion-selective Zn-ZIF-62 glass protective layer and g) the assembly of LMO-1-g//MOC-1 full cell. h) The cycling performance (inset: the digital photo of the LED experiment for LMO-1-g) in LIB full cells at 1 C, i) rate capability, and j) Ragone plots for LMO-1-g, LMO-1, and LMO-S. k) The HAADF-STEM image of LMO-1-g after 150 cycles in the LIB full cell.

(e.g., Mn₃O₄, Li₄Mn₅O₁₂, Li₂Mn₂O₄) can be detected in LMO-1-g, thereby elucidating the inhibited structural failure and smaller capacity attenuation.^[60] The crack formation of electrodes is another useful metric for the structural integrity of spinel materials. Upon cycling, the Jahn-Teller effect-induced phase transition results in the strengthened local strain between the lithiated surface and the bulk material, especially during fast discharging, thereby intensifying the collapse of the local microstructure and promoting crack formation.^[65,68] The ex situ SEM images after 2500 cycles at 5 C illustrate the suppressed structural deterioration of LMO-1-g in contrast to LMO-1 with a smaller density of mechanical cracks (Figure 6d; Figure S47, Supporting Information). Bestowed by the mitigated mechanical stress due to the

inhibition of Jahn-Teller distortion in LMO-1-g, the mechanical cracks can be reduced compared with LMO-1, contributing to the exalted structural robustness and prolonged cycle life.^[65] Additionally, the structural integrity of the glassy coating layer was studied with the aid of ex situ TEM (Figure S48, Supporting Information), where the non-crystalline protective layer can be found. The composition of the protective layer and the retention of the MOF structure during cycling were further verified by the near-edge X-ray absorption fine structure (NEXAFS) spectra (Figure S49, Supporting Information). In the Zn *L*-edge spectra, the major peaks located at low-energy and high-energy regions correspond to the Zn 2p_{3/2} and Zn 2p_{1/2}, respectively.^[72] These remain unchanged in the crystal Zn-ZIF-62 and the Zn-ZIF-62 glass layer

after cycling. The N K-edge spectra for the crystal Zn-ZIF-62 and the Zn-ZIF-62 glass layer also show similar traits, where the peak intensity reduces in the Zn-ZIF-62 glass layer due to the local breakage of Zn–N bonds.^[30] These observations jointly corroborate the preservation of the MOF structure in Zn-ZIF-62 after vitrification and cycling, indicating its functionality as a robust protective shell. To quantify the Mn²⁺ loss during the cycling process, inductively coupled plasma (ICP) spectrometry was utilized. Consequently, LMO-1-g outperformed LMO-1 in Mn retention rate during the cycling test at 1 C (Figure 6e), further supporting the effectiveness of the Zn-ZIF glass layer in the suppression of Mn²⁺ dissolution. Based on the above observations, the functionality of the protective layer in LMO-1-g is displayed in Figure 6f, where the Zn-ZIF-62 glass shield serves as a protective layer to allow Li⁺ penetration and thwart Mn²⁺ dissolution, thereby warranting fast Li⁺ diffusion and reducing Mn²⁺ loss. This dexterously circumvents the Jahn-Teller distortion brought by oxygen vacancy engineering.

To embody the practicability of the above strategy, the full cell assembly with LMO products as cathodes and MOC intermediates as anodes was attempted (Figure 6g). Before full-cell measurements, the half-cell measurements of MOC-1, MOC-2, and MOC-3 were executed. MOC-1 surpassed its counterparts in reversible capacity, rate capability, and charge/ion transfer kinetics (Figures S50–S58, Supporting Information), which can be ascribed to the successive conductive network, elastic carbon matrix, and optimal morphological properties endowed by the MOF template.^[34,35] Based on the above comparison, MOC-1 was selected as the anode material in full-cell measurements. LMO-1-g performed steadily in the LIB full cell with a reversible capacity of 120.9 mAh g⁻¹ at 1 C (88% retention) after 150 cycles, profoundly outperforming LMO-1 and LMO-S (Figure 6h). Impressively, the light-emitting diode (LED) can be lighted by the LMO-1-g//MOC-1 after the cycling test, further supporting the potential of LMO-1-g in practical LIB systems. The more distinct and stable voltage plateaus and the smaller voltage decay of LMO-1-g (Figure S59, Supporting Information) substantiate its outstanding structural robustness in LIB full cells caused by the stabilization effect of the Zn-ZIF-62 glass layer.^[73] During the rate performance test, LMO-1-g manifested superior reversible capacities (144.9, 132.9, 107.1, 80.6, 62.7 mAh g⁻¹ at 0.5, 1, 2, 5, and 10 C, respectively) and more stable voltage platforms (Figure 6i; Figure S60, Supporting Information), demonstrating its expedited lithium storage kinetics. The long-term cycling measurement at 2 C (85.5 mAh g⁻¹ after 150 cycles with a capacity retention of 85%) further highlights the capability of LMO-1-g as a longevous cathode in LIB full cells (Figure S61, Supporting Information). Considering the significance of energy/power densities for practical battery systems, the Ragone plots are disclosed in Figure 6j, where the significant superiority of LMO-1-g in energy density and power density is emphasized, thereby excavating its great application potential.^[54]

The electrochemical kinetics of LMO-1-g in LIB full cells were explored to understand the role of the Zn-ZIF-62 glass shield. The EIS study of LIB full cells (Figure S62, Supporting Information) shows the much smaller R_{ct} values of LMO-1-g and LMO-1 compared with LMO-S, illustrating the predominant advantage of the self-sacrificial templated route in structural optimization toward ameliorated full cell performances. In addi-

tion, LMO-1 exerted a much more significant increase in the R_{ct} value compared with LMO-1-g after 150 cycles at 1 C. This elucidates the boosted charge transfer kinetics in LMO-1-g induced by the substantial lithium ion conductivity of the Zn-ZIF-62 glass and the stabilized electrode/electrolyte interface.^[27,29] During the CV measurement at 0.2 mV s⁻¹ (Figure S63, Supporting Information), the smaller peak-to-peak separation of the LMO-1-g//MOC-1 full cell suggests its favorable electrochemical kinetics brought by the enhanced structural reversibility and the mitigated Jahn-Teller effect.^[7] The lithium storage behaviors in LIB full cells were further quantitatively analysed by pseudocapacitive calculations. As expected, the LMO-1-g//MOC-1 full cell exerted higher pseudocapacitive contribution compared with the LMO-1//MOC-1 full cell (Figure S64, Supporting Information), manifesting the accelerated lithium diffusion owing to the more stable surface structure and the inhibition of detrimental heterophase formation.^[12,25] To verify this deduction from the atomic level, the spherical aberration-corrected high-angle annular dark-field scanning transmission electron microscopy (HAADF-STEM) was implemented. It's acknowledged that the formation of Mn₃O₄ surface layer (namely, "bad spinel") formation can reflect the occurrence of the Jahn-Teller effect and cause the blockage of Li⁺ diffusion pathways.^[23] Therefore, the thickness of Mn₃O₄ surface layers is a crucial factor in evaluating the local structural integrity and electrochemical activity retention in spinel materials. As delivered in Figure 6k, a ~2.5 nm Mn₃O₄ region is formed in LMO-1-g after 150 cycles at 1 C in the full cell. In contrast, a thicker Mn₃O₄ layer (~4 nm) was observed in LMO-1, accompanied by the more pronounced Li/Mn exchange (Figure S65, Supporting Information), thereby revealing the intensified surface structural evolution and internal structure destruction within LMO-1 due to the Mn²⁺ loss and the unrecoverable "bad spinel".^[12,25] In light of the above observations, the Zn-ZIF-62 glass shield effectively mitigates the Mn²⁺ dissolution without blocking Li⁺ transport, increases the stability of surface/inner structures within spinel LiMn₂O₄, and hence imparts LMO-1-g with desirable electrochemical kinetics and extended cycle life in LIB half/full cells. Coupled with the optimal morphological/crystal features and the oxygen-deficient nature, LMO-1-g delivered significantly enhanced performance as a longevous LIB cathode.

3. Conclusion

In summary, we elaborately optimized and modified LiMn₂O₄ by combining the MOF-templated route and Zn-ZIF-62 glass coating. The smart selection of MOF precursors imparted LiMn₂O₄ with desirable morphological features, uniform particle growth, satisfying crystallinity degree, and a proper amount of oxygen defects. These advantageous factors jointly contributed to the superior lithium storage property of LMO-1 derived from Mn-BDC. Enlightened by experimental and computational results, it can be deduced that the existence of oxygen defects can boost the electronic/ion transport, thereby resulting in remarkable reversible capacities, impressive multiplier behavior, and accelerated electrochemical kinetics. Furthermore, the utilisation of glassy Zn-ZIF-62 shield effectively evaded the drawbacks of oxygen defects in LiMn₂O₄ including the increased amount of Mn³⁺ ions and aggravated Jahn-Teller distortion. It's noteworthy that the

Zn-ZIF-62 glass layer successfully confined Mn²⁺ in the spinel structure without blocking aisles for Li⁺ transmission, thereby strengthening the structural reversibility and prolonging the lifespan with negligible sacrifice in reversible capacity. The intermarriage of oxygen defects and Zn-ZIF-62 glass led to stable lithium storage capacities in LIB half cell (120.6 mAh g⁻¹ at 1 C for 500 cycles; 83.7 mAh g⁻¹ at 5 C for 2500 cycles) and full cell (120.9 and 85.5 mAh g⁻¹ after 150 cycles at 1 C and 2 C, respectively), which opens an avenue for the practical application of the oxygen-deficient LiMn₂O₄ as a longevous LIB cathode.

Supporting Information

Supporting Information is available from the Wiley Online Library or from the author.

Acknowledgements

J.-E.Z., Y.L., M.Z., and X.H. contributed equally to this work. We gratefully acknowledge the financial support from the National Natural Science Foundation of China (52302283) and the Shanghai Pujiang Program (No. 24PJA034). Furthermore, the authors would like to thank the Shiyanjia lab (<https://www.shiyanjia.com>) for the TEM test.

Conflict of Interest

The authors declare no conflict of interest.

Data Availability Statement

The data that support the findings of this study are available from the corresponding author upon reasonable request.

Keywords

LiMn₂O₄ cathode, metal-organic framework, oxygen defect, zeolitic imidazolate framework glass

Received: January 17, 2025

Revised: April 6, 2025

Published online:

- [1] L. Ben, J. Zhou, H. Ji, H. Yu, W. Zhao, X. Huang, *Mater. Futures* **2021**, *1*, 015101.
- [2] R. Liu, N. Li, E. Zhao, J. Zhao, L. Yang, W. Wang, H. Liu, C. Zeng, *Mater. Futures* **2022**, *1*, 045102.
- [3] C. Zheng, S. Tang, F. Wen, J. Peng, W. Yang, Z. Lv, Y. Wu, W. Tang, Z. Gong, Y. Yang, *Mater. Futures* **2022**, *1*, 045103.
- [4] Y. Luo, Q. Pan, H. Wei, Y. Huang, L. Tang, Z. Wang, C. Yan, J. Mao, K. Dai, Q. Wu, X. Zhang, J. Zheng, *Adv. Energy Mater.* **2023**, *13*, 2300125.
- [5] M. Huang, M. Wang, L. Yang, Z. Wang, H. Yu, K. Chen, F. Han, L. Chen, C. Xu, L. Wang, P. Shao, X. Luo, *Nano-Micro Lett.* **2024**, *16*, 207.
- [6] M. Jeong, M. J. Lee, J. Cho, S. Lee, *Adv. Energy Mater.* **2015**, *5*, 1500440.
- [7] B. Tao, L. C. Yule, E. Daviddi, C. L. Bentley, P. R. Unwin, *Angew. Chem., Int. Ed.* **2019**, *58*, 4606.
- [8] Y. Guo, X. Li, Z. Wang, J. Wang, H. Guo, G. Yan, *J. Energy Chem.* **2022**, *73*, 452.
- [9] S. Lee, Y. Cho, H. K. Song, K. T. Lee, J. Cho, *Angew. Chem., Int. Ed.* **2012**, *51*, 8748.
- [10] H. Zhang, Z. Huang, L. Zhao, Z. Guo, J. Wang, J. Liu, Y. Zhao, F. Li, P. Zhang, Z.-Y. Ji, *Chem. Eng. J.* **2024**, *482*, 148802.
- [11] Q. Qu, L. Fu, X. Zhan, D. Samuelis, J. Maier, L. Li, S. Tian, Z. Li, Y. Wu, *Energy Environ. Sci.* **2011**, *4*, 3985.
- [12] S. Zhang, H. Chen, J. Chen, S. Fang, L. Ni, H. Wang, W. Deng, G. Zou, H. Hou, X. Ji, *Adv. Funct. Mater.* **2023**, *33*, 2210731.
- [13] G. Tan, S. Wan, J. J. Chen, H. Q. Yu, Y. Yu, *Adv. Mater.* **2024**, *36*, 2310657.
- [14] W. Xu, Y. Zheng, L. Lin, W. Lei, Z. Wang, H. Song, Y. Cheng, R. Qi, H. Peng, H. Lin, Z. Yang, R. Huang, *J. Alloys Compd.* **2021**, *870*, 159387.
- [15] W. Zhu, J. Zhang, J. Luo, C. Zeng, H. Su, J. Zhang, R. Liu, E. Hu, Y. Liu, W. D. Liu, Y. Chen, W. Hu, Y. Xu, *Adv. Mater.* **2023**, *35*, 2208974.
- [16] S. Wang, S. Jiang, Y. Li, Z. Tan, S. Hao, J. Yang, Z. He, *J. Power Sources* **2023**, *579*, 233292.
- [17] J. Sun, H. X. Liu, T. F. Liu, *Chin. J. Struct. Chem.* **2021**, *40*, 1082.
- [18] H. H. Tan, L. V. Xiao-Long, J. L. Liu, Y. F. Cheng, Q. L. Zhou, Y. T. Lin, W. Meng, *Chin. J. Struct. Chem.* **2021**, *40*, 459.
- [19] C.-P. Wan, J.-D. Yi, R. Cao, Y.-B. Huang, *Chin. J. Struct. Chem.* **2022**, *41*, 2205001.
- [20] T. De Villenoisy, X. Zheng, V. Wong, S. S. Mofarah, H. Arandiyan, Y. Yamauchi, P. Koshy, C. C. Sorrell, *Adv. Mater.* **2023**, *35*, 2210166.
- [21] C. Yin, Z. Bao, H. Tan, H. Zhou, J. Li, *Chem. Eng. J.* **2019**, *372*, 408.
- [22] Z. L. Chen, Y. J. Gu, Y. L. Huo, X. Y. Ma, F. Z. Wu, *J. Alloys Compd.* **2022**, *917*, 165485.
- [23] Y. Huang, Y. Dong, S. Li, J. Lee, C. Wang, Z. Zhu, W. Xue, Y. Li, J. Li, *Adv. Energy Mater.* **2020**, *11*, 2000997.
- [24] X. Hou, X. Liu, H. Wang, X. Zhang, J. Zhou, M. Wang, *Energy Storage Mater.* **2023**, *57*, 577.
- [25] D. Tang, Y. Sun, Z. Yang, L. Ben, L. Gu, X. Huang, *Chem. Mater.* **2014**, *26*, 3535.
- [26] R. E. Warburton, M. J. Young, S. Letourneau, J. W. Elam, J. Greeley, *Chem. Mater.* **2020**, *32*, 1794.
- [27] W. Zhang, X. Sun, Y. Tang, H. Xia, Y. Zeng, L. Qiao, Z. Zhu, Z. Lv, Y. Zhang, X. Ge, S. Xi, Z. Wang, Y. Du, X. Chen, *J. Am. Chem. Soc.* **2019**, *141*, 14038.
- [28] L. L. De Taeye, I. Teirllynck, P. M. Vereecken, *Adv. Funct. Mater.* **2021**, *31*, 2105180.
- [29] G. Jiang, C. Qu, F. Xu, E. Zhang, Q. Lu, X. Cai, S. Hausdorf, H. Wang, S. Kaskel, *Adv. Funct. Mater.* **2021**, *31*, 2104300.
- [30] C. Gao, Z. Jiang, S. Qi, P. Wang, L. R. Jensen, M. Johansen, C. K. Christensen, Y. Zhang, D. B. Ravnsbæk, Y. Yue, *Adv. Mater.* **2022**, *34*, 2110048.
- [31] Y. Song, Y. Ren, H. Cheng, Y. Jiao, S. Shi, L. Gao, H. Xie, J. Gao, L. Sun, J. Hou, *Angew. Chem., Int. Ed.* **2023**, *62*, 202306420.
- [32] J. Ding, T. Du, L. R. Jensen, S. S. Sørensen, D. Wang, S. Wang, L. Zhang, Y. Yue, M. M. Smedskjaer, *Adv. Mater.* **2024**, *36*, 2400652.
- [33] J. Yan, C. Gao, S. Qi, Z. Jiang, L. R. Jensen, H. Zhan, Y. Zhang, Y. Yue, *Nano Energy* **2022**, *103*, 107779.
- [34] L. Fan, X. Guo, W. Li, X. Hang, H. Pang, *Chin. Chem. Lett.* **2023**, *34*, 107447.
- [35] L. Zhao, J. Feng, A. Abbas, C. Wang, H. Wang, *Small* **2023**, *19*, 2302953.
- [36] S. Wu, C. Yuan, Z. Huang, H. Xu, W. Shen, *Chem. Eng. J.* **2024**, *479*, 147928.
- [37] Y. Wang, L. Feng, W. Fan, K. Y. Wang, X. Wang, X. Wang, K. Zhang, X. Zhang, F. Dai, D. Sun, H. C. Zhou, *J. Am. Chem. Soc.* **2019**, *141*, 6967.
- [38] A. P. Chernyshev, *Mater. Chem. Phys.* **2022**, *282*, 125979.
- [39] M. Choi, W. Lee, *Chem. Eng. J.* **2022**, *431*, 134345.
- [40] S. J. Clark, M. D. Segall, C. J. Pickard, P. J. Hasnip, M. I. J. Probert, K. Refson, M. C. Payne, *Z. Kristallogr.* **2005**, *220*, 567.

- [41] J. P. Perdew, K. Burke, M. Ernzerhof, *Phys. Rev. Lett.* **1996**, *77*, 3865.
- [42] G. Zhang, M. Chen, C. Li, B. Wu, J. Chen, W. Xiang, X. Wen, D. Zhang, G. Cao, W. Li, *Chem. Eng. J.* **2022**, *443*, 136434.
- [43] Y. Ren, J. He, S. Jiang, R. He, Q. Liang, B. Zhu, Y. Wen, S. Zhuang, *Mater. Lett.* **2024**, *357*, 135765.
- [44] Y. Chen, B. Xi, M. Huang, L. Shi, S. Huang, N. Guo, D. Li, Z. Ju, S. Xiong, *Adv. Mater.* **2022**, *34*, 2108621.
- [45] Y. Liu, T. Zhou, Y. Zheng, Z. He, C. Xiao, W. K. Pang, W. Tong, Y. Zou, B. Pan, Z. Guo, Y. Xie, *ACS Nano* **2017**, *11*, 8519.
- [46] Y. Sun, L. Zan, Y. Zhang, *Appl. Surf. Sci.* **2019**, *483*, 270.
- [47] R. Huang, Y. H. Ikuhara, T. Mizoguchi, S. D. Findlay, A. Kuwabara, C. A. J. Fisher, H. Moriwake, H. Oki, T. Hirayama, Y. Ikuhara, *Angew. Chem., Int. Ed.* **2011**, *50*, 3053.
- [48] X. Li, W. Huang, A. Krajnc, Y. Yang, A. Shukla, J. Lee, M. Ghasemi, I. Martens, B. Chan, D. Appadoo, P. Chen, X. Wen, J. A. Steele, H. G. Hackbarth, Q. Sun, G. Mali, R. Lin, N. M. Bedford, V. Chen, A. K. Cheetham, L. H. G. Tizei, S. M. Collins, L. Wang, J. Hou, *Nat. Commun.* **2023**, *14*, 7612.
- [49] R. Lin, X. Li, A. Krajnc, Z. Li, M. Li, W. Wang, L. Zhuang, S. Smart, Z. Zhu, D. Appadoo, J. R. Harmer, Z. Wang, A. G. Buzanich, S. Beyer, L. Wang, G. Mali, T. D. Bennett, V. Chen, J. Hou, *Angew. Chem., Int. Ed.* **2022**, *61*, 202112880.
- [50] T. D. Bennett, S. Horike, *Nat. Rev. Mater.* **2018**, *3*, 431.
- [51] A. Qiao, T. D. Bennett, H. Tao, A. Krajnc, G. Mali, C. M. Doherty, A. W. Thornton, J. C. Mauro, G. N. Greaves, Y. Yue, *Sci. Adv.* **2018**, *4*, aao6827.
- [52] O. Smirnova, S. Hwang, R. Sajzew, L. Ge, A. Reupert, V. Nozari, S. Savani, C. Chmelik, M. R. Reithofer, L. Wondraczek, J. Kärger, A. Knebel, *Nat. Mater.* **2024**, *23*, 262.
- [53] J. Lin, E. Fan, X. Zhang, Z. Li, Y. Dai, R. Chen, F. Wu, L. Li, *Adv. Energy Mater.* **2022**, *12*, 2201174.
- [54] Y. Wang, X. Zhao, J. Jin, Q. Shen, Y. Hu, X. Song, H. Li, X. Qu, L. Jiao, Y. Liu, *J. Am. Chem. Soc.* **2023**, *145*, 22708.
- [55] Y. L. Ding, J. Xie, G. S. Cao, T. J. Zhu, H. M. Yu, X. B. Zhao, *Adv. Funct. Mater.* **2011**, *21*, 348.
- [56] J. Abou-Rjeily, I. Bezza, N. A. Laziz, C. Autret-Lambert, M. T. Sougrati, F. Chamouss, *Energy Storage Mater.* **2020**, *26*, 423.
- [57] L. Jaber-Ansari, K. P. Puntambekar, S. Kim, M. Aykol, L. Luo, J. Wu, B. D. Myers, H. Iddir, J. T. Russell, S. J. Saldaña, R. Kumar, M. M. Thackeray, L. A. Curtiss, V. P. Dravid, C. Wolverton, M. C. Hersam, *Adv. Energy Mater.* **2015**, *5*, 1500646.
- [58] R. Thirunakaran, G. H. Lew, W.-S. Yoon, *J. Energy Chem.* **2017**, *26*, 101.
- [59] L. Gou, Y.-F. Zhang, W. Wang, J.-Y. Ying, X.-Y. Fan, Z.-Z. Zhang, *Chem. Eng. J.* **2024**, *498*, 155755.
- [60] S. Zhang, H. Chen, J. Chen, S. Yin, Y. Mei, L. Ni, A. Di, W. Deng, G. Zou, H. Hou, X. Ji, *J. Energy Chem.* **2022**, *72*, 379.
- [61] J.-E. Zhou, H. Zhong, Y. Zhang, Q. Huang, B. Zhang, A. Zeb, Z. Xu, X. Lin, *Chem. Eng. J.* **2022**, *450*, 137448.
- [62] K. Nakajima, F. L. Souza, A. L. M. Freitas, A. Thron, R. H. R. Castro, *Chem. Mater.* **2021**, *33*, 3915.
- [63] T. D. Bennett, Y. Yue, P. Li, A. Qiao, H. Tao, N. G. Greaves, T. Richards, G. I. Lampronti, S. A. T. Redfern, F. Blanc, O. K. Farha, J. T. Hupp, A. K. Cheetham, D. A. Keen, *J. Am. Chem. Soc.* **2016**, *138*, 3484.
- [64] C. W. Ashling, D. N. Johnstone, R. N. Widmer, J. Hou, S. M. Collins, A. F. Sapnik, A. M. Bumstead, P. A. Midgley, P. A. Chater, D. A. Keen, T. D. Bennett, *J. Am. Chem. Soc.* **2019**, *141*, 15641.
- [65] Z. Guo, H. Jiang, X. Sun, X. Li, Z. Liu, J. Zhang, J. Luo, J. Zhang, X. S. Tao, J. Ding, X. Han, R. Liu, Y. Chen, W. Hu, *Adv. Energy Mater.* **2024**, *14*, 2302484.
- [66] S. Dong, L. Shi, S. Geng, Y. Ning, C. Kang, Y. Zhang, Z. Liu, J. Zhu, Z. Qiang, L. Zhou, G. Yin, D. Li, T. Mu, S. Lou, *Nano-Micro Lett.* **2024**, *17*, 95.
- [67] C. Yin, H. Zhou, Z. Yang, J. Li, *ACS Appl. Mater. Interfaces* **2018**, *10*, 13625.
- [68] S. Lee, G. Yoon, M. Jeong, M. J. Lee, K. Kang, J. Cho, *Angew. Chem., Int. Ed.* **2015**, *54*, 1153.
- [69] L. Song, S. Zhang, L. Duan, R. Li, Y. Xu, J. Liao, L. Sun, X. Zhou, Z. Guo, *Angew. Chem., Int. Ed.* **2024**, *63*, 202405648.
- [70] E. Kim, J. Lee, J. Park, H. Kim, K. W. Nam, *Nano Lett.* **2025**, *25*, 619.
- [71] W. Zeng, F. Xia, J. Wang, J. Yang, H. Peng, W. Shu, Q. Li, H. Wang, G. Wang, S. Mu, J. Wu, *Nat. Commun.* **2024**, *15*, 7371.
- [72] S. Ghosh, S. Nandy, A. Valalahally Gopala, T. K. Patra, K. H. Chae, B. R. K. Nanda, C. Sudakar, *ACS Appl. Mater. Interfaces* **2025**, *17*, 9460.
- [73] Q. Li, C. Yang, J. Zhang, X. Ji, J. Xu, X. He, L. Chen, S. Hou, J. Uddin, D. Addison, D. Sun, C. Wang, F. Wang, *Angew. Chem., Int. Ed.* **2022**, *61*, 202214126.